Generalized Haldane model in a magneto-optical honeycomb lattice

Mark J. Ablowitz [1] and Justin T. Cole [2]
[1]*Department of Applied Mathematics, University of Colorado, Boulder, Colorado 80309, USA*
[2]*Department of Mathematics, University of Colorado, Colorado Springs, Colorado 80918, USA*

(Received 3 February 2023; revised 17 September 2023; accepted 26 January 2024; published 4 March 2024)

A two-dimensional honeycomb lattice composed of gyrotropic rods is studied. Beginning with Maxwell's equations, a perturbed Wannier method is used to derive a tight-binding model with nearest and next-nearest neighbors. The resulting discrete model leads to a generalized (photonic) Haldane model that supports topologically protected modes with nonzero Chern numbers. Varying the radii of the rods breaks inversion symmetry and can change the topology of the system. This model analytically describes experimental results associated with topological waves in magneto-optical honeycomb lattices. This method can also be applied to more general Chern insulator lattices. When on-site Kerr-type nonlinear effects are considered, coherent soliton-like modes are found to propagate robustly through boundary defects.

DOI: 10.1103/PhysRevA.109.033503

I. INTRODUCTION

The study of topological insulators is an area of research currently receiving significant interest. These types of systems can be experimentally realized in numerous fields including ultracold fermionic systems [1], semiconductors [2,3], magnetic media [4], equatorial waves [5], and electromagnetic systems [6–8]. Underlying these works are topologically protected states that are robust to defects.

This work focuses on topological insulators that are distinguished by bulk eigenmodes with a nontrivial Chern number. In this case, the bulk-edge correspondence implies the existence of topologically protected modes. Indeed, these systems can support edge states that propagate unidirectionally around the boundary with or without material defects.

A standard approach for describing topological insulator lattice systems is a tight-binding model. Typically, tight-binding models consist of a set of discrete equations that reduce the complexity of the governing equations, yet still capture the essential behavior. Moreover, it is common in experiments for the dielectric contrast in photonic waveguides to naturally reside in the deep lattice regime, which is central in the tight-binding approximation [9,10].

One of the most well-known and heavily studied topological insulator systems is the *Haldane model* [11], associated with honeycomb lattices. This relatively simple model, which includes nearest- and next-nearest-neighbor interactions, is able to capture the essence of Chern insulator systems. The model illustrates that breaking of time-reversal symmetry is necessary for realizing bulk modes with nontrivial Chern topological invariants. Moreover, when inversion symmetry is broken in an appropriate manner exceeding that of time-reversal symmetry, a topological transition to a trivial Chern system can take place.

While Ref. [11] offers no derivation for the model, it effectively describes the behavior of the quantum Hall effect in honeycomb lattices. Indeed, many authors have applied the Haldane model to describe systems with nonzero Chern numbers. For instance, electron gases with an electrostatic honeycomb potential behave as a massless Dirac system near the Dirac points [12]. Applying an external magnetic field is capable of gapping the system, which can then be described by the Haldane model [13]. Haldane models have also been used to describe electromagnetic systems with pseudo-Tellegen effects [14]. In addition, periodically driven ultracold fermionic systems or photonic honeycomb lattices can also yield Haldane-type models in a high-frequency limit [1,15]. In the latter cases, the periodic driving creates an effective magnetic field.

This work provides a direct derivation of a generalized Haldane model from Maxwell's equations in a magneto-optical (MO) system. The physical system considered here is that of transverse magnetic (TM) waves in a ferrimagnetic photonic crystal with an applied external magnetic field, which is a photonic analog of the quantum Hall effect. To our knowledge, this is the first time a tight-binding model has been formulated for this system. These TM systems have been realized in both square [16–19] and honeycomb [20–23] lattices and found to support topologically protected edge modes. Topologically protected modes in EM systems were originally proposed by Haldane and Raghu [24,25] and their existence studied in Ref. [26]. Our work shows a direct derivation of a Haldane-type model from gyrotropic systems.

The key to our approach is the use of a suitable Wannier basis in which to expand the EM field [27]. Unfortunately, a direct Wannier expansion is ineffective due to nontrivial topology, which is the result of a discontinuity in the spectral phase of the associated Bloch function [15,28]. As a result, the corresponding Wannier-Fourier coefficients do not decay rapidly. Seeking a tight-binding model in a basis of these slowly decaying Wannier modes would require many interactions, well beyond nearest neighbor, to accurately describe the problem. Consequently, this would cease to be an effective reduction of the original problem.

By considering nearest- and next-nearest-neighbor interactions, a Haldane model is derived from the original MO

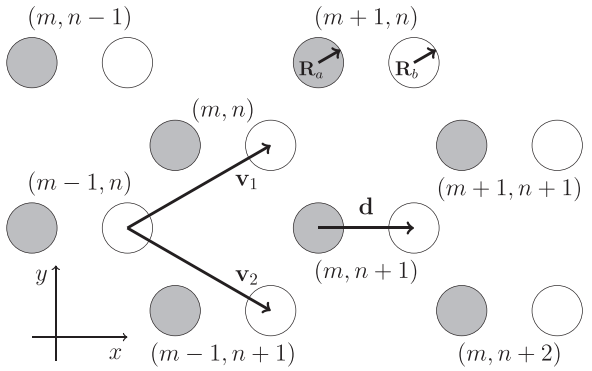

FIG. 1. Planar honeycomb array of ferrite rods. The lattice a sites (b sites) are gray (white) disks with radius R_a (R_b). A constant magnetic field $H_0\hat{\mathbf{z}}$ is applied. The indices (m, n) denote integer shifts in the $\mathbf{v}_1$ and $\mathbf{v}_2$ directions, respectively. The displacement between two rods in the same cell is $\mathbf{d}$ with $||\mathbf{d}||_2 = \ell$.

honeycomb lattice. With physically relevant parameters, an analytical study of the system topology is conducted. The topological transition points are identified and found to agree well with numerical approximations. Nontrivial Chern numbers are found to correspond to unidirectional chiral modes.

The Wannier basis method we use was applied to a square MO lattice in Ref. [27]. The results in this paper show that the method is effective, again. This approach can be applied to other systems, e.g., different lattices, governed by the TM equation with gyrotropic lattices. We expect this method to be effective in other Chern insulator systems as well.

We also examine the effect of nonlinearity on edge mode propagation. Edge solitons, unidirectional nonlinear envelopes that balance nonlinearity and dispersion, have been explored in Floquet Chern insulator systems [29,30,31]. The work of Ref. [32] showed that significant amounts of radiation are emitted from the solitary wave for highly localized (nonlinear) envelopes.

The nonlinear system we consider is a Haldane model that includes on-site Kerr nonlinearity. A similar system has also been derived from a nonlinear Floquet system in a high-frequency driving limit [15]. Different nonlinear Haldane models with saturable nonlinearity [33] and mass terms [34] have previously been explored. Slowly varying and balanced envelopes are observed to propagate coherently and robustly around lattice boundaries. Due to their ability to balance nonlinear and dispersive effects, while localized along the boundary, we call these edge solitons.

II. MAGNETO-OPTICAL SYSTEM

The setup we consider is a planar array $\mathbf{r} = (x, y)^T$ of ferrimagnetic, e.g., yttrium iron garnet (YIG), rods arranged in a honeycomb lattice pattern (see Fig. 1). Similar designs were implemented in Refs. [16,17] and [20,22]. The parallelogram unit cell contains an a site and b site with radii of R_a and R_b, respectively. All other cells are integer translations of the lattice vectors

$$\mathbf{v}_1 = \ell\begin{pmatrix} \frac{3}{2} \\ \frac{\sqrt{3}}{2} \end{pmatrix}, \quad \mathbf{v}_2 = \ell\begin{pmatrix} \frac{3}{2} \\ -\frac{\sqrt{3}}{2} \end{pmatrix}$$

from the unit cell, where ℓ is the distance between nearest-neighbor rods. The notation (m, n) indicates a rod that is displaced $m\mathbf{v}_1 + n\mathbf{v}_2$ away from the unit cell, where $m, n \in \mathbb{Z}$.

A constant external magnetic field is applied in the perpendicular (out of the page) direction, $H_0\hat{\mathbf{z}}$, and induces a saturated magnetic response. For time-harmonic fields with angular frequency ω, the ferrite rods induce the gyrotropic permeability tensor [35]

$$[\mu] = \begin{pmatrix} \mu & i\kappa & 0 \\ -i\kappa & \mu & 0 \\ 0 & 0 & \mu_0 \end{pmatrix}, \tag{1}$$

where $\mu = \mu_0(1 + \frac{\omega_0\omega_m}{\omega_0^2 - \omega^2})$ and $\kappa = \mu_0\frac{\omega\omega_m}{\omega_0^2 - \omega^2}$. The coefficients are defined in terms of $\omega_0 = \mu_0\gamma H_0$ and $\omega_m = \mu_0\gamma 4\pi M_s$, where μ_0 is the vacuum permeability, γ is the gyromagnetic ratio, and M_s is the magnetization saturation of the material.

For rods with permittivity $\varepsilon(\mathbf{r})$, the governing TM wave equation for a time-harmonic field is

$$-\nabla^2 E + \mathcal{M}\cdot\nabla E = \omega^2\varepsilon\tilde{\mu}E,$$
$$\mathcal{M}(\mathbf{r}) = \nabla\ln\tilde{\mu} - i\tilde{\mu}(\hat{\mathbf{z}}\times\nabla\eta), \tag{2}$$

where E, plus its complex conjugate, is the z component of the electric field, $\tilde{\mu} = \frac{\mu^2 - \kappa^2}{\mu}$, and $\eta = -\frac{\kappa}{\mu^2 - \kappa^2}$. Here, we take a nondispersive approximation and fix the values of μ and κ: ω is fixed to eventual band-gap frequencies. For a typical YIG rod at frequency $f = 7.7$ GHz ($f = \omega/2\pi$) with saturation magnetization $4\pi M_s = 1750$ G and magnetizing field $H_0 = 500$ Oe, the constitutive relations are approximately $\mu = 0.88\mu_0$, $\kappa = -0.66\mu_0$, and $\varepsilon = 15\varepsilon_0$. The equation is nondimensionalized via $\mathbf{r} \to \ell\mathbf{r}$, $\mu \to \mu_0\mu$, $\kappa \to \mu_0\kappa$, $\varepsilon \to \varepsilon_0\varepsilon$, $\omega \to c\omega/\ell$, where c is the speed of light and $\varepsilon_0 = (c^2\mu_0)^{-1}$ is the vacuum permittivity.

The coefficients in (2) share the translation symmetry of the honeycomb lattice: $\varepsilon(\mathbf{r} + m\mathbf{v}_1 + n\mathbf{v}_2) = \varepsilon(\mathbf{r})$, $\tilde{\mu}(\mathbf{r} + m\mathbf{v}_1 + n\mathbf{v}_2) = \tilde{\mu}(\mathbf{r})$, and $\eta(\mathbf{r} + m\mathbf{v}_1 + n\mathbf{v}_2) = \eta(\mathbf{r})$, where $m, n \in \mathbb{Z}$. Bloch theory motivates bulk wave solutions of the form $E(\mathbf{r};\mathbf{k}) = e^{i\mathbf{k}\cdot\mathbf{r}}u(\mathbf{r};\mathbf{k})$, with $u(\mathbf{r} + m\mathbf{v}_1 + n\mathbf{v}_2;\mathbf{k}) = u(\mathbf{r};\mathbf{k})$ for quasimomentum $\mathbf{k}$, where the reciprocal lattice vectors are given by

$$\mathbf{k}_1 = \frac{2\pi}{\ell}\begin{pmatrix} \frac{1}{3} \\ \frac{1}{\sqrt{3}} \end{pmatrix}, \quad \mathbf{k}_2 = \frac{2\pi}{\ell}\begin{pmatrix} \frac{1}{3} \\ -\frac{1}{\sqrt{3}} \end{pmatrix}.$$

The second term in $\mathcal{M}(\mathbf{r})$ is induced by the external magnetic field and is responsible for breaking time-reversal symmetry. Moreover, this term is directly proportional to the associated vector potential [16]

$$\mathcal{A}(\mathbf{r}) = \frac{\tilde{\mu}}{2}(\hat{\mathbf{z}}\times\nabla\eta), \tag{3}$$

which corresponds to the effective or induced magnetic flux density $\mathcal{B}(\mathbf{r}) = \nabla\times\mathcal{A}(\mathbf{r}) = \frac{\hat{\mathbf{z}}}{2}(\nabla\tilde{\mu}\cdot\nabla\eta + \tilde{\mu}\nabla^2\eta)$. From the point of view of the Schrödinger equation with a magnetic field, $\mathcal{B}$ plays the role of a "photonic" magnetic field. That is, it is different from the actual (physical) magnetic field given by $\mathbf{B} = [\mu]\mathbf{H}$. When deriving our generalized Haldane model

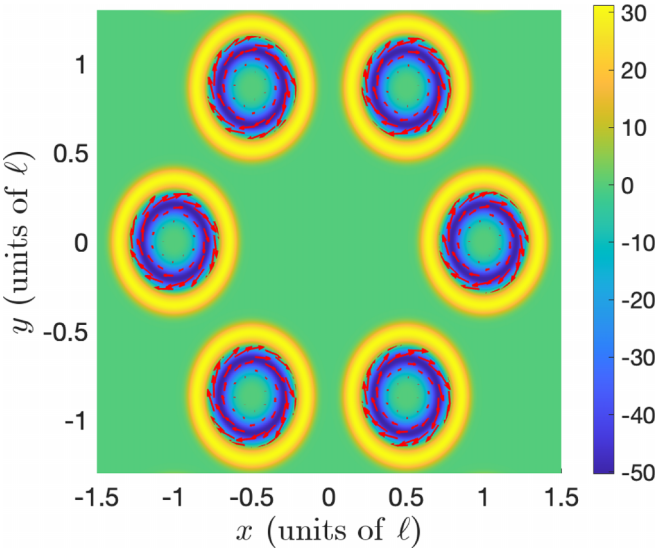

FIG. 2. The region indicated by the colorbar is the effective magnetic flux density $\mathcal{B}(\mathbf{r}) \cdot \hat{\mathbf{z}}$ for ferrite rods with $R_a = R_b = 0.3\ell$. Superimposed on top is the vector potential $\mathcal{A}(\mathbf{r})$ in (3). The vector potential (indicated by red arrows) circulates clockwise near the ferrite-air boundary.

below, the induced magnetic field is the more useful quantity; we will refer to it as the effective magnetic field.

A typical magnetic potential and effective magnetic field are shown in Fig. 2. Similar to the original Haldane model [11], here the magnetic flux through the unit cell is observed to be zero, that is, $\iint_{\mathrm{UC}} \mathcal{B}(\mathbf{r}) \cdot \hat{\mathbf{z}}\, dS = 0$; this was verified numerically. The vector potential consists of localized circulations along the boundary of the rods, due to the gradient term in (3). The circulations have a clockwise orientation about rod centers and appear to only have angular motion (no radial component). As such, the magnetic flux $\mathcal{A}(\mathbf{l}) \cdot d\mathbf{l}$, where $\mathbf{l}$ is a radially oriented path from the center of one rod to the center of the next-nearest neighbor, is identically zero, unlike the original Haldane model [11]. Nonetheless, the topological nature of the discrete model derived below is related to the magnetic potential shown in Fig. 2.

Solving the resulting equation for $[u(\mathbf{r};\mathbf{k}), \omega(\mathbf{k})]$, via spectral methods along the $\Gamma MK\Gamma$ path in $\mathbf{k}$-space (see Appendix A), we obtain the two lowest spectral bands shown in Fig. 3. The location of Dirac points (up to integer translations of the reciprocal lattice vectors) are

$$K' = \begin{pmatrix} 0 \\ \frac{4\pi}{3\sqrt{3}\ell} \end{pmatrix}, \quad K = \begin{pmatrix} 0 \\ -\frac{4\pi}{3\sqrt{3}\ell} \end{pmatrix}.$$

In Fig. 3(a), no external magnetic field is applied and a conical Dirac point is observed at the K point. When a magnetic field is applied, then $\mathcal{M}$ is nonzero, time-reversal symmetry is broken, and a band gap opens [see Fig. 3(b)]. Moreover, there is an associated set of nonzero Chern numbers. Note that the first (lowest) band is denoted by "–" subscript, while the second band is denoted by "+" subscript. In Fig. 3 we also compare with the discrete-tight binding approximation discussed below.

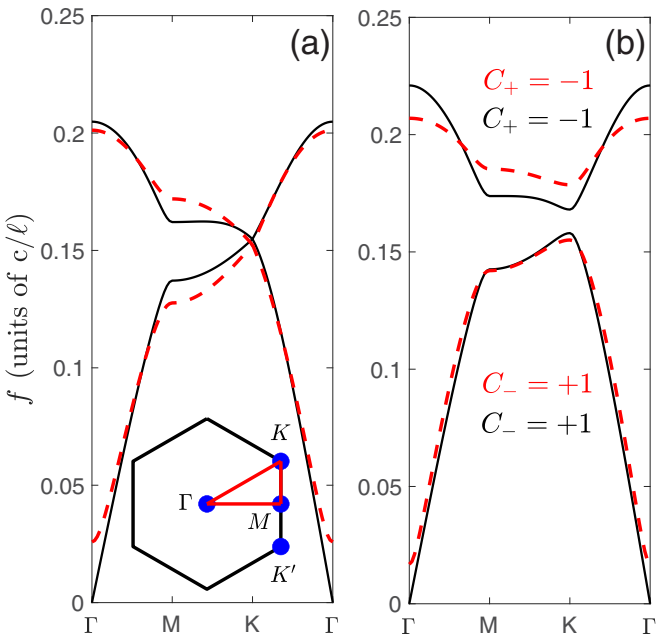

FIG. 3. Normalized frequency bands obtained by solving (2) for $u(\mathbf{r};\mathbf{k}) = e^{-i\mathbf{k}\cdot\mathbf{r}} E(\mathbf{r};\mathbf{k})$ for values of $\mathbf{k}$ along the path $\Gamma MK\Gamma$ with $R_a = R_b = 0.3\ell$. Shown are the first two bands (ascending order) for (a) nonmagnetized ($\mathcal{M} = \mathbf{0}$, $\tilde{\mu} = \mu_0$) and (b) magnetized ($\mathcal{M} \neq \mathbf{0}$, $\tilde{\mu} \neq \mu_0$) systems. Solid lines indicate numerically computed curves. Dashed lines denote the tight-binding approximation. Chern numbers are the same for both.

III. A PERTURBED WANNIER APPROACH

A strong dielectric contrast between the rods and background motivates a tight-binding approximation, whereby a variable coefficient partial differential equation (PDE) with a periodic lattice potential, i.e., (2), can be reduced to a constant coefficient system of ordinary differential equations (ODEs) [9]. Bloch wave solutions of (2) are periodic with respect to the quasimomentum $\mathbf{k}$: $E(\mathbf{r};\mathbf{k} + m\mathbf{k}_1 + n\mathbf{k}_2) = E(\mathbf{r};\mathbf{k})$, where the reciprocal lattice vectors $\mathbf{k}_{1,2}$ satisfy $\mathbf{v}_i \cdot \mathbf{k}_j = 2\pi\delta_{ij}$. As such, the Bloch wave can be expanded in a Fourier in $\mathbf{k}$ series

$$E(\mathbf{r};\mathbf{k}) = \sum_p \sum_{m,n} W^p_{mn}(\mathbf{r}) e^{i\mathbf{k}\cdot(m\mathbf{v}_1 + n\mathbf{v}_2)}, \tag{4}$$

where W^p_{mn} denotes the Wannier function corresponding to the (m, n) spatial cell and p^{th} spectral band.

Due to the properties of Fourier coefficients, the decay of $W^p_{mn}(\mathbf{r})$ depends on the smoothness of $E(\mathbf{r};\mathbf{k})$ in $\mathbf{k}$. Chern insulators possess an essential phase discontinuity that cannot be removed via gauge transformation [28]. As a result, a direct Wannier expansion is not useful. A closely related set of exponentially localized Wannier functions, which come from a problem *with* time-reversal symmetry [27], can be used perturbatively.

Consider (2) with $\mathcal{M} = \mathbf{0}$, but $\tilde{\mu} \neq \mu_0$—the so-called "perturbed problem." The maximally localized Wannier (MLWF) functions, found using well-known methods [36], corresponding to the first two Wannier functions, called $\widetilde{W}^a_{mn}(\mathbf{r})$ and $\widetilde{W}^b_{mn}(\mathbf{r})$, are shown in Fig. 4 and are centered at

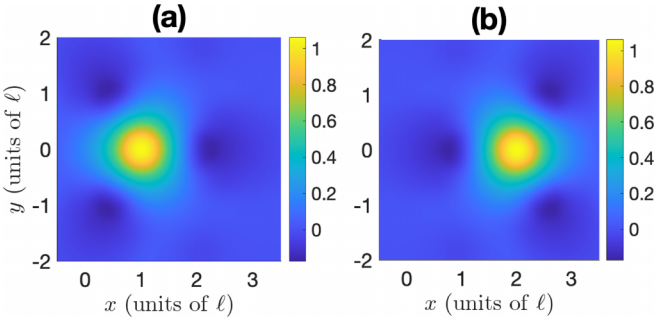

FIG. 4. Maximally localized Wannier functions (a) $\widetilde{W}^a_{00}(\mathbf{r})$ and (b) $\widetilde{W}^b_{00}(\mathbf{r})$, obtained from (2) when $\mathcal{M} = \mathbf{0}$, $\tilde{\mu} \neq \mu_0$, and $R_a = R_b = 0.3\ell$.

the a sites $(\mathbf{d} + m\mathbf{v}_1 + n\mathbf{v}_2)$ and b sites $(2\mathbf{d} + m\mathbf{v}_1 + n\mathbf{v}_2)$, respectively. These Wannier functions are related to those in (4) (when $\mathcal{M} = \mathbf{0}$) by a unitary transformation chosen to minimize the spread (see Appendix C). Note that these functions are real, exponentially localized, and approximately exhibit the mirror symmetry about the $x = 3\ell/2$ axis; i.e., $\widetilde{W}^a_{00}(-(\mathbf{r} - 3\ell\hat{\mathbf{x}}/2)) = \widetilde{W}^b_{00}(\mathbf{r} - 3\ell\hat{\mathbf{x}}/2)$.

The Bloch wave is expanded in terms of this new basis,

$$E(\mathbf{r};\mathbf{k}) = \sum_{m,n} \left[a_{mn}\widetilde{W}^a_{mn}(\mathbf{r}) + b_{mn}\widetilde{W}^b_{mn}(\mathbf{r})\right], \tag{5}$$

where all phases have been absorbed in the coefficients. Properly normalized Wannier modes exhibit the orthogonality property $\langle W^p_{mn}, W^{p'}_{m'n'}\rangle_{\mathbb{R}^2} = \delta_{mm'}\delta_{nn'}\delta_{pp'}$ for the weighted inner product $\langle f, g\rangle_{\mathbb{R}^2} = \int\int_{\mathbb{R}^2} f(\mathbf{r})^* g(\mathbf{r})\varepsilon(\mathbf{r})\tilde{\mu}(\mathbf{r})d\mathbf{r}$.

Substituting (5) into (2) with $\mathcal{M} \neq 0$, multiplying by $\widetilde{W}^j_{mn}(\mathbf{r})$, $j = a, b$, and integrating over $\mathbb{R}^2$ yields a system of algebraic equations whose coefficients depend on integrals over perturbed Wannier functions. Once the MLWFs are obtained, these integrals are numerically approximated. Since this is a deep lattice, only nearby interactions are kept since the others are small. We keep terms up to the next-nearest-neighboring sites.

IV. A HALDANE-TYPE MODEL

A tight-binding model is obtained by substituting the Wannier expansion (5) into the governing equation (2) and then numerically approximating the relevant overlap integrals (see Ref. [27] for more details on the method). The precise coefficient definitions are given in Appendix B. Inspection of the numerically computed tight-binding coefficients (see Appendix A) reveals an effective discrete approximation that is a generalization of the well-known Haldane model [11]. Namely, replacing ω by id/dt, we obtain the key equations of this work,

$$\frac{d^2a_{mn}}{dt^2} + Pa_{mn} + t_1(\delta_- b_{mn}) + t_2e^{i\phi}(\Delta_1 a_{mn}) + t_2e^{-i\phi}(\Delta_2 a_{mn}) = 0, \tag{6}$$

$$\frac{d^2b_{mn}}{dt^2} + \widetilde{P}b_{mn} + t_1(\delta_+ a_{mn}) + \tilde{t}_2e^{-i\phi}(\Delta_1 b_{mn}) + \tilde{t}_2e^{i\phi}(\Delta_2 b_{mn}) = 0, \tag{7}$$

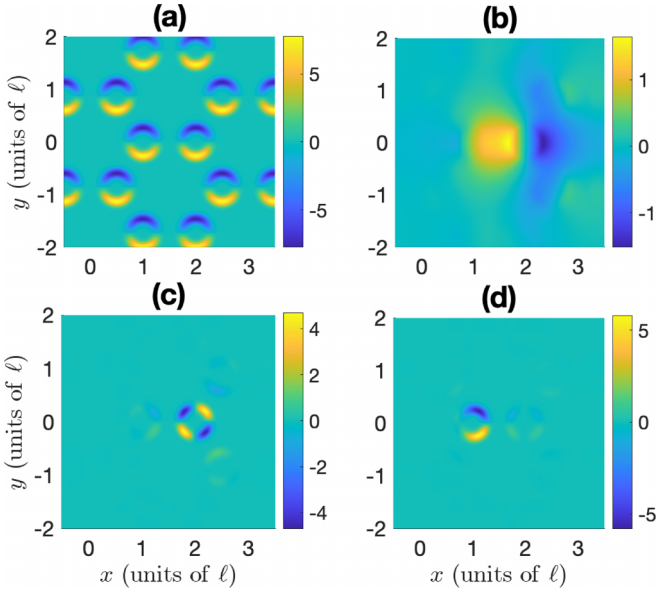

FIG. 5. Illustration of why $\mathrm{Im}\{P\} = \mathrm{Im}\{\widetilde{P}\} = 0$ and $\mathrm{Im}\{t_1\} = 0$. (a) $\mathrm{Im}\{\hat{\mathbf{x}}\cdot\mathcal{M}\}$, (b) $\partial\widetilde{W}^b_{00}/\partial x$, (c) $\mathrm{Im}\{\widetilde{\mathrm{W}}^{\mathrm{b}}_{00}(\hat{\mathbf{x}}\cdot\mathcal{M})\frac{\partial\widetilde{\mathrm{W}}^{\mathrm{b}}_{00}}{\partial x}\}$ [product of Fig. 4(b) and panels (a) and (b)], and (d) $\mathrm{Im}\{\widetilde{\mathrm{W}}^{\mathrm{a}}_{00}(\hat{\mathbf{x}}\cdot\mathcal{M})\frac{\partial\widetilde{\mathrm{W}}^{\mathrm{b}}_{00}}{\partial x}\}$ [product of Fig. 4(a) and panels (a) and (b)]. A similar study shows that the y-component counterparts of (c) and (d) are also odd. The imaginary part of P and t_1 is obtained by integrating (c) and (d), respectively (and their y counterparts), revealing a null imaginary part. Note that $P = \widetilde{P}$ here.

where $(\delta_\pm c_{mn}) \equiv c_{mn} + c_{m\pm1,n} + c_{m,n\pm1}$ are the nearest-neighbor interactions and $(\Delta_1 c_{mn}) \equiv c_{m,n+1} + c_{m-1,n} + c_{m+1,n-1}$ and $(\Delta_2 c_{mn}) \equiv c_{m+1,n} + c_{m,n-1} + c_{m-1,n+1}$ are next-nearest-neighbor contributions, such that $c = a$ or $c = b$. The parameters $P, \widetilde{P}, t_1, t_2, \tilde{t}_2, \phi$ are real-valued numbers; these values depend on the physical quantities μ, κ, ε and sizes of the radii of the rods.

Here, the external magnetic field ($H_0 \neq 0$) is found to induce complex ($\phi \neq 0$) next-nearest coefficients, but real self ($P, \widetilde{P}$) and nearest (t_1) neighbor terms. Upon closer inspection of the imaginary part of $\widetilde{P}$ and t_1 [see Eqs. (B2) and (B3) in Appendix B, respectively], we find local symmetries cause its elimination. This is highlighted in Fig. 5. For example, the imaginary part of $\hat{\mathbf{x}}\cdot\mathcal{M}$ is odd in the y direction at each rod [see Fig. 5(a)], while $\partial\widetilde{W}^b_{mn}/\partial x$ is (approximately) odd about b-site rods in the x direction [see Fig. 5(b)]. Multiplying these functions by $\widetilde{W}^b_{mn}$ [Fig. 4(b)] and $\widetilde{W}^a_{mn}$ [Fig. 4(a)] yields the imaginary x component of the self [Fig. 5(c)] and nearest [Fig. 5(d)] neighbor contributions, respectively. The corresponding tight-binding coefficients are obtained by integrating these functions. Then, integration yields a net zero contribution due to the local odd symmetries. The y-component portion behaves in a similar manner.

The complex nature of the next-nearest-neighbor coefficients defined in (B4) (in Appendix B) is a direct result of the vector potential (3), which appears in the coefficient $\mathcal{M}(\mathbf{r})$ in (2). Moreover, it is related to the intrinsic honeycomb lattice symmetry. A more thorough examination of the next-nearest-neighbor interactions is outside the scope of this work.

TABLE I. Tight-binding parameters in (6) and (7) for different applied external magnetic field strengths. The other physical parameters used are $R_a = R_b = 0.3\ell$, $\varepsilon = 15\varepsilon_0$, and $4\pi M_s = 1750$ G, at frequency $f = 7.7$ GHz. All cases have the same topological number.

H_0 (Oe)	P	t_1	t_2	ϕ
300	0.982	−0.276	0.029	2.314
400	0.998	−0.278	0.034	2.317
500	1.020	−0.280	0.041	2.327
600	1.058	−0.285	0.052	2.346
700	1.103	−0.293	0.062	2.358

Notice that this system reduces to the "classical" Haldane model given in Ref. [11] when $\tilde{t}_2 = t_2$ and $\phi \to -\phi$. The equations can be put in a more standard form by looking for solutions of the form $a_{mn} \to a_{mn}e^{i\omega t}$, similarly for b_{mn}, and then shifting the spectrum $\omega^2 \to \omega^2 + (P + \widetilde{P})/2$. This yields an on-site inversion parameter

$$M \equiv \frac{P - \widetilde{P}}{2}, \tag{8}$$

which is important in Ref. [11] and below. The result of this latter spectral shift is to effectively replace P by M in (6) and $\widetilde{P}$ by $-M$ in (7).

We find the classical Haldane model when inversion symmetry is *not* broken ($P = \widetilde{P}, t_2 = \tilde{t}_2$) and a modified version when inversion symmetry *is* broken ($P \neq \widetilde{P}, t_2 \neq \tilde{t}_2$). For instance, when the a-site and b-site rods differ, the inversion symmetry of the lattice, $\mathbf{r} \to -\mathbf{r}$, is broken, and this leads to different interactions among the Wannier modes and hence different coefficients (see Sec. V and Appendix C).

We compare the bulk bands of the discrete model to those numerically computed from (2); see Fig. 3. (All tight-binding parameters used can be found in Appendix B.) Indeed, the discrete approximation shows good agreement with the numerical bands; the relative error throughout the Brillouin zone is 6.5% or less. Moreover, for $\ell = 5.8$ mm spacing, the gap frequencies in Fig. 3(b) lie in the vicinity of the 8-GHz microwave regime observed in Ref. [22].

To gain insight into the physical nature of the parameter ϕ, we perform two tests. First, dependence on the applied magnetic field is explored. The value of H_0 is varied while the material parameters, e.g., ε and M_s, are held fixed [cf. Eq. (1)]. The parameters are shown in Table I. Since inversion symmetry is not broken, $P = \widetilde{P}$ and $\tilde{t}_2 = t_2$. Examining the model parameters, we observe that the magnitudes of the P, t_1, and t_2 parameters increase, with little (effectively no) change to the phase parameter ϕ. For saturated magnetic ferrites, there is little change in the values of μ and κ since ω is well separated from the resonant frequency ω_0 here.

Next, we consider a scenario in (1) where μ is fixed and the value of κ is varied independently of it. The results are shown in Fig. 6. When $\kappa = 0$ all the nearest- and next-nearest-neighbor coefficients are real and negative, hence $\phi = \pi$. As κ decreases and approaches $-\mu$, the value of ϕ also decreases. Moreover, it is clear that the value of ϕ

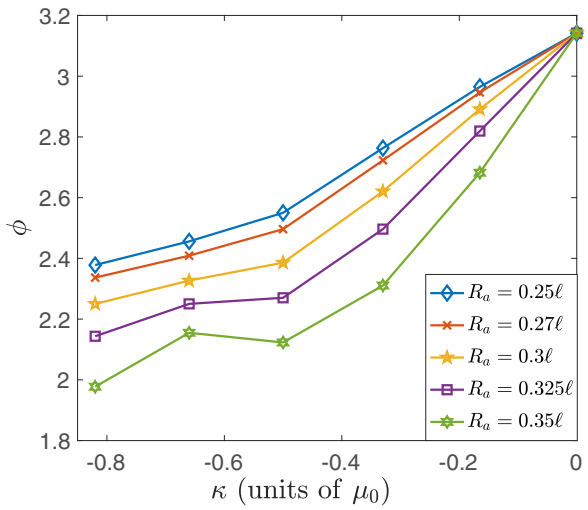

FIG. 6. Dependence of the phase parameter ϕ in (6) and (7) on the anisotropy parameter κ in (1) for $\mu = 0.88\mu_0$ and $R_b = 0.3\ell$.

depends on the rod radii, R_a and R_b. This is not surprising since the Wannier functions often reflect the physical profile of the photonic medium [15]. Therefore, as the radius of the rod changes, so does the vector potential and the phase parameter ϕ. If the direction of the magnetic field is changed, i.e., $H_0 \to -H_0, M_s \to -M_s$, then (1) is effectively conjugated and the phase terms in (6) and (7) reverse sign, i.e., $\phi \to -\phi$.

Reviewing the results of these tests, we can say that the range of values for $t_2 e^{i\phi}$ and $\tilde{t}_2 e^{i\phi}$ primarily reside in the second quadrant of the complex plane. Changing the direction of the external physical magnetic field changes the direction of the vector potential field $\mathcal{A}(\mathbf{r})$ and conjugates these coefficients into the third quadrant. Hence, many values inside $\pi/2 < |\phi| < \pi$ in the phase diagram in Fig. 7 are realized by adjusting κ and μ.

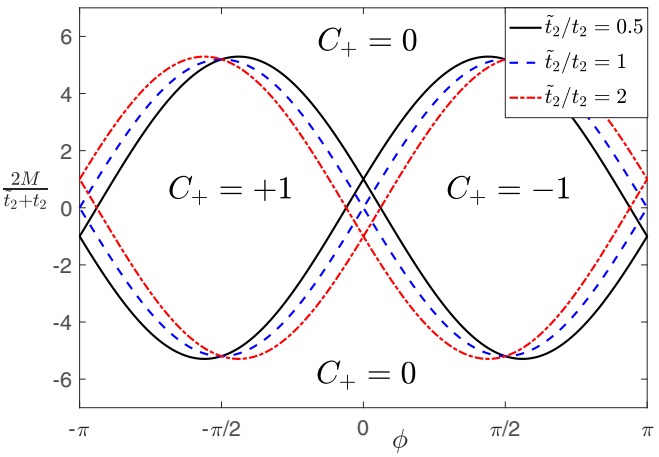

FIG. 7. Phase diagram separating nontrivial Chern insulator (interior) and trivial (exterior) systems for different ratios of $\tilde{t}_2/t_2$. Shown is the Chern number C_+ for the second spectral band; the signs are reversed for C_- corresponding to the first band.

V. ANALYTICAL CALCULATION OF BULK MODES

Consider bulk plane wave solutions of system (6) and (7) with the form

$$a_{mn}(t) = \alpha(\mathbf{k})e^{i[\mathbf{k}\cdot(m\mathbf{v}_1+n\mathbf{v}_2)+\omega(\mathbf{k})t]},$$
$$b_{mn}(t) = \beta(\mathbf{k})e^{i[\mathbf{k}\cdot(m\mathbf{v}_1+n\mathbf{v}_2)+\omega(\mathbf{k})t]},$$

where $\mathbf{k} \in \mathbb{R}$. Next, define the nearest- and next-nearest-neighbor vectors $\mathbf{a}_1 = \mathbf{0}, \mathbf{a}_2 = \mathbf{v}_1, \mathbf{a}_3 = \mathbf{v}_2$, and $\mathbf{b}_1 = \mathbf{v}_1, \mathbf{b}_2 = -\mathbf{v}_2, \mathbf{b}_3 = \mathbf{v}_2 - \mathbf{v}_1$, respectively. Then, the bulk Haldane system can be expressed as the following eigenvalue problem:

$$\begin{pmatrix} M + H_0 + H_3 & H_1 - iH_2 \\ H_1 + iH_2 & -M + \tau(H_0 - H_3) \end{pmatrix}\begin{pmatrix}\alpha \\ \beta\end{pmatrix} = \widetilde{\omega}^2\begin{pmatrix}\alpha \\ \beta\end{pmatrix}, \tag{9}$$

where $\tau = \tilde{t}_2/t_2 > 0$ and $M = (P - \widetilde{P})/2$ with the terms

$$H_0(\mathbf{k}) = 2t_2\cos\phi\sum_{j=1}^{3}\cos(\mathbf{k}\cdot\mathbf{b}_j)$$
$$H_1(\mathbf{k}) = t_1\sum_{j=1}^{3}\cos(\mathbf{k}\cdot\mathbf{a}_j)$$
$$H_2(\mathbf{k}) = t_1\sum_{j=1}^{3}\sin(\mathbf{k}\cdot\mathbf{a}_j)$$
$$H_3(\mathbf{k}) = 2t_2\sin\phi\sum_{j=1}^{3}\sin(\mathbf{k}\cdot\mathbf{b}_j).$$

Note that we have utilized the frequency shift $\omega^2 = \widetilde{\omega}^2 + (P + \widetilde{P})/2$ to follow the convention used in Ref. [11]. When $\tau = 1$, this is precisely Haldane's model [11] when $\phi \to -\phi$ and $\widetilde{\omega}^2 \to \overline{\omega}^2 + H_0$. The dispersion surfaces of (9) are given by

$$\widetilde{\omega}^2_{\pm}(\mathbf{k}) = \frac{H_0(\mathbf{k})(1+\tau) + H_3(\mathbf{k})(1-\tau)}{2} \pm \sqrt{H_1(\mathbf{k})^2 + H_2(\mathbf{k})^2 + \frac{1}{4}[2M + H_0(\mathbf{k})(1-\tau) + H_3(\mathbf{k})(1+\tau)]^2}. \tag{10}$$

Below, we begin by studying the behavior of the spectrum near the Dirac points. In the absence of magnetization ($\phi = \pi$) the spectral gap closes and the bands $\widetilde{\omega}_{\pm}$ touch at these points. Moreover, as will be explained below, the contributions that result in nonzero Chern numbers are acquired at these points.

Consider the behavior of the spectral bands in (10) at the Dirac point $K' = (0, \frac{4\pi}{3\sqrt{3}\ell})^T$, where the functions H_j, $j = 0, ..., 3$ reduce to

$$H_0(K') = -3t_2\cos\phi, \quad H_1(K') = 0,$$
$$H_2(K') = 0, \quad H_3(K') = 3\sqrt{3}t_2\sin\phi.$$

Hence, at this Dirac point, the spectral bands in (10) are given by

$$\widetilde{\omega}^2_{\pm} = \frac{-3t_2\cos\phi(1+\tau) + 3\sqrt{3}t_2\sin\phi(1-\tau)}{2} \pm \frac{1}{2}|2M - 3t_2\cos\phi(1-\tau) + 3\sqrt{3}t_2\sin\phi(1+\tau)|.$$

A gap closure (i.e., $\widetilde{\omega}_+ = \widetilde{\omega}_-$) occurs when the equation

$$2M - 3(t_2 - \tilde{t}_2)\cos\phi + 3\sqrt{3}(t_2 + \tilde{t}_2)\sin\phi = 0 \tag{11}$$

is satisfied.

If, on the other hand, the Dirac point $K = -K'$ is considered, then

$$H_0(K) = -3t_2\cos\phi, \quad H_1(K) = 0,$$
$$H_2(K) = 0, \quad H_3(K) = -3\sqrt{3}t_2\sin\phi,$$

where the only difference is the sign of H_3. Here, the corresponding gap closure occurs when the equation

$$2M - 3(t_2 - \tilde{t}_2)\cos\phi - 3\sqrt{3}(t_2 + \tilde{t}_2)\sin\phi = 0 \tag{12}$$

is satisfied. When $\tau = 1\,(M = 0)$ (inversion symmetry present), the gap closure condition reduces to that of the classical Haldane model: $\phi = n\pi$ with $n \in \mathbb{Z}$. The curves in (11) and (12) are shown in Fig. 7 for different values of τ and correspond to topological transition points.

The eigenmodes associated with the $\widetilde{\omega}^2_{\pm}$ eigenvalues in (10) are

$$\mathbf{c}_{\pm}(\mathbf{k}) = \frac{1}{D(\mathbf{k})}\begin{pmatrix} H_1(\mathbf{k}) - iH_2(\mathbf{k}) \\ \widetilde{\omega}^2_{\pm}(\mathbf{k}) - M - H_0(\mathbf{k}) - H_3(\mathbf{k}) \end{pmatrix}. \tag{13}$$

The term $D(\mathbf{k})$ is a normalization factor chosen to ensure $||\mathbf{c}_{\pm}||_2 = 1$. Notice that these functions are periodic in $\mathbf{k}$: $\mathbf{c}_{\pm}(\mathbf{k} + \mathbf{k}_j) = \mathbf{c}_{\pm}(\mathbf{k})$ for the reciprocal lattice vectors $j = 1, 2$.

The Chern numbers are given by

$$C_{\pm} = \frac{1}{2\pi i}\iint_{\Omega}\left(\left\langle\frac{\partial\mathbf{c}_{\pm}}{\partial k_x}, \frac{\partial\mathbf{c}_{\pm}}{\partial k_y}\right\rangle - \left\langle\frac{\partial\mathbf{c}_{\pm}}{\partial k_y}, \frac{\partial\mathbf{c}_{\pm}}{\partial k_x}\right\rangle\right)d\mathbf{k}, \tag{14}$$

where $\langle\mathbf{f}, \mathbf{g}\rangle = \mathbf{f}^{\dagger}\mathbf{g}$ and $\dagger$ indicates the complex conjugate transpose. The region Ω is a reciprocal unit cell, given by the parallelogram region formed by the reciprocal lattice vectors $\mathbf{k}_1, \mathbf{k}_2$.

To compute (14), Stokes' theorem is applied over Ω. This equates the double integral over Ω to a closed line integral along the boundary $\partial\Omega$. However, since the eigenfunctions (13) are not differentiable at the Dirac points, a contour integral which excludes these points must be implemented (see Ref. [15]). Due to the periodic boundary conditions in the

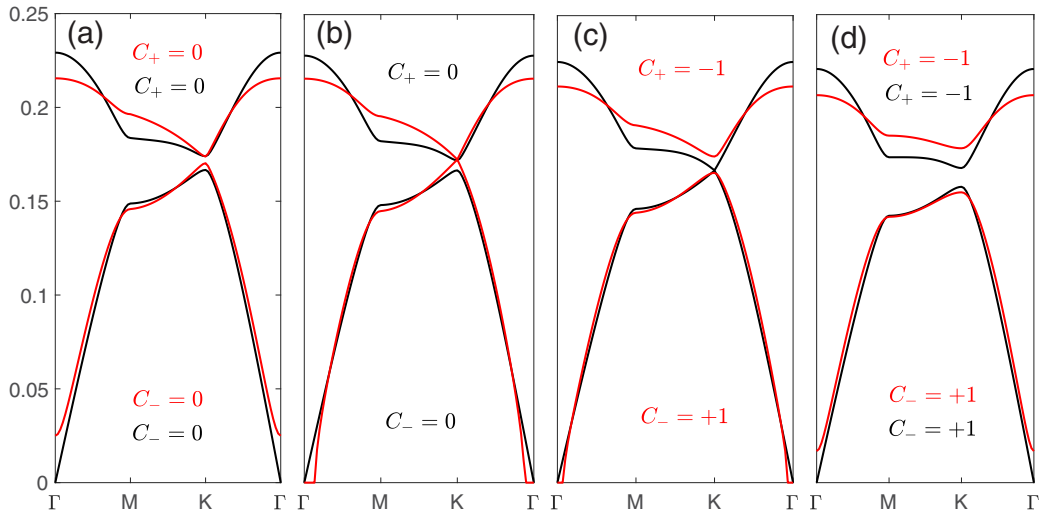

FIG. 8. Topological transition of frequency Bloch bands as inversion symmetry is broken by decreasing the radius R_a while keeping $R_b = 0.3\ell$. Numerical (black curves) and tight-binding (red curves) approximations are shown for (a) $R_a = 0.25\ell$, (b) $R_a = 0.255\ell$, (c) $R_a = 0.27\ell$, and (d) $R_a = 0.3\ell$.

eigenmodes, the boundary $\partial\Omega$ makes no contribution to the Chern number. The only nontrivial contributions come from the two Dirac points,

$$C_\pm = -\frac{1}{2\pi i}\oint_{\partial K} \mathbf{A}_\pm(\mathbf{k})\cdot d\mathbf{k} - \frac{1}{2\pi i}\oint_{\partial K'} \mathbf{A}_\pm(\mathbf{k})\cdot d\mathbf{k}, \quad (15)$$

where $\mathbf{A}_\pm(\mathbf{k}) = \langle \mathbf{c}_\pm, \nabla_\mathbf{k}\mathbf{c}_\pm\rangle = \langle \mathbf{c}_\pm, \partial_{k_x}\mathbf{c}_\pm\rangle\widehat{k}_x + \langle \mathbf{c}_\pm, \partial_{k_y}\mathbf{c}_\pm\rangle\widehat{k}_y$ is the Berry connection. The contours of integration in (15) are taken to be small counterclockwise oriented circles centered around the Dirac points, K and K', respectively.

Next, the eigenmodes are linearized about the Dirac point $\mathbf{k} = K'$; a similar calculation follows for the other Dirac point. Doing so, we get

$$\mathbf{c}_\pm(\mathbf{k}) \approx \mathbf{c}_\pm(K') + (\mathbf{k} - K')\cdot\nabla_\mathbf{k}\mathbf{c}_\pm(K'),$$

where $\nabla_\mathbf{k} \equiv \partial_{k_x}\widehat{k}_x + \partial_{k_y}\widehat{k}_y$. After renormalizing the linear approximation via $\psi = \mathbf{c}_\pm/||\mathbf{c}_\pm||_2$, the Berry connection and Chern number (14) are computed in the neighborhood of the K' Dirac point.

The following are the results. The contribution to the total Chern number at the K' Dirac point is -1 for

$$2M - 3(t_2 - \tilde{t}_2)\cos\phi + 3\sqrt{3}(t_2 + \tilde{t}_2)\sin\phi > 0, \quad (16)$$

and 0 otherwise. Meanwhile, the contribution at the K Dirac point is $+1$ for

$$2M - 3(t_2 - \tilde{t}_2)\cos\phi - 3\sqrt{3}(t_2 + \tilde{t}_2)\sin\phi > 0, \quad (17)$$

and 0 otherwise. The combination of these regions of topology is summarized in Fig. 7. This figure represents a generalization of the phase diagram in Ref. [11].

The Chern number is found by combining the contributions in (16) and (17). Suppose we focus on the interval $0 < \phi < \pi$. Then, for parameters that satisfy neither (16) nor (17), that is, $2M < 3(t_2 - \tilde{t}_2)\cos\phi - 3\sqrt{3}(t_2 + \tilde{t}_2)\sin\phi$, both Dirac points have zero contribution and $C_+ = 0 + 0 = 0$. Next, for values that satisfy (16), but not (17), the K' Dirac point contributes -1, and the K point has a null contribution, so $C_+ = -1 + 0 = -1$. Lastly, when both (16) and (17) are satisfied, that is, $2M > 3(t_2 - \tilde{t}_2)\cos\phi + 3\sqrt{3}(t_2 + \tilde{t}_2)\sin\phi$, both Dirac points contribute and cancel each other out, so $C_+ = -1 + 1 = 0$. For all cases considered in this paper, the analytically computed Chern numbers agree with numerics [37].

Lastly, it is observed that, similar to the classic Haldane model, band gaps associated with topologically protected waves only open for $\phi \neq n\pi$, $n \in \mathbb{Z}$. Physically, values of $\phi = n\pi$ correspond to completely real next-nearest-neighbor coefficients. Opening a spectral gap that supports topologically protected edge modes requires complex next-nearest-neighbor coefficients. In this model, the complex nature of the next-nearest-neighbor coefficients is induced by the external magnetic field.

A. Broken inversion symmetry

A notable feature of the Haldane model is a change in topology when the degree to which the inversion symmetry is broken is sufficiently large. The generalized model (6) and (7) also exhibits this property. Physically, inversion symmetry of the system can be broken by choosing different radii for the a and b lattice sites, that is, $R_a \neq R_b$. Doing so leads to $P \neq \widetilde{P}$, $t_2 \neq \tilde{t}_2$, and $M \neq 0$ [as defined in (8)].

Spectral band diagrams resulting from such a change are shown in Figs. 8 and 9. As the radii differential changes, the system undergoes a topological transition that is captured by the model. We observe that when R_a is sufficiently smaller (or larger) than R_b, the system is a trivial Chern insulator. Only when $R_a \approx R_b$ do we observe a nontrivial Chern insulator state.

Specifically, for fixed radius $R_b = 0.3\ell$, the (numerical) transition points between a trivial and nontrivial Chern insulator occur at approximately $R_a = 0.27\ell$ [at $k = K$; see Fig. 8(c)] and $R_a = 0.35\ell$ [at $k = K'$; see Fig. 9(b)]. The discrete model (6) and (7) is also found to exhibit these topological transitions when the inversion symmetry is broken. On the other hand, the bands of the discrete model close at slightly

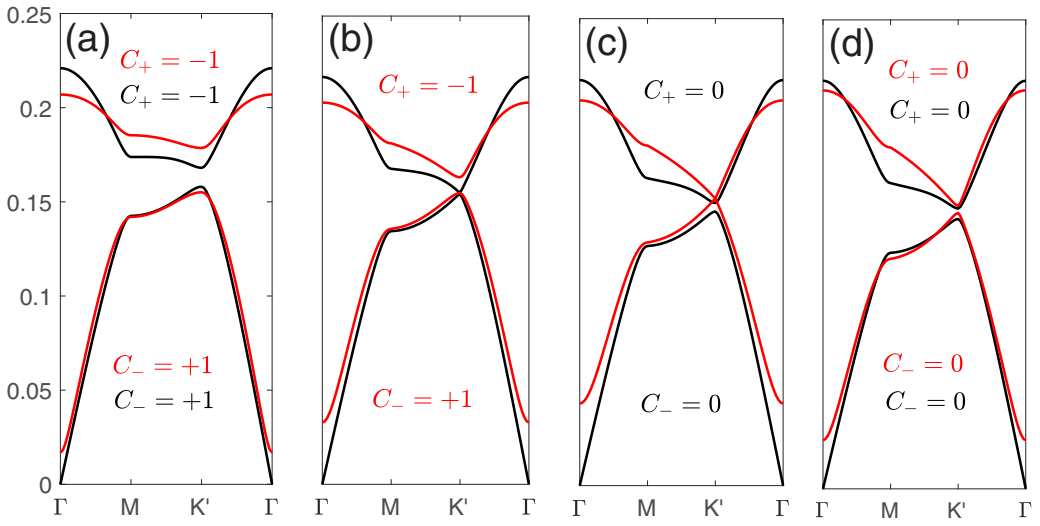

FIG. 9. Spectral bands and topological transition when inversion symmetry is broken by increasing the radius R_a while fixing $R_b = 0.3\ell$. Numerical (black curves) and tight-binding (red curves) approximations are shown for (a) $R_a = 0.3\ell$, (b) $R_a = 0.35\ell$, (c) $R_a = 0.4\ell$, and (d) $R_a = 0.42\ell$.

different radii, namely, (approximately) $R_a = 0.255\ell$ [at $k = K$; see Fig. 8(b)] and $R_a = 0.4\ell$ [at $k = K'$; see Fig. 9(c)]. To reduce this discrepancy, more accurate approximations can be obtained by adding more interactions, e.g., next-next-nearest neighbor.

We note that for values of τ smaller than 1, like Fig. 8, typically the difference $|R_a - R_b|$ for $R_a < R_b$ needs to be smaller to see a topological transition (numerical bands touch for $R_a = 0.27\ell, R_b = 0.3\ell$, so $|R_a - R_b| = 0.03\ell$). In contrast, when $R_a > R_b$ and τ is larger than 1, like Fig. 9, a larger difference $|R_a - R_b|$ is needed for a topological transition (numerical bands touch for $R_a = 0.35\ell, R_b = 0.3\ell$, so $|R_a - R_b| = 0.05\ell$).

The tight-binding model also exhibits this asymmetry. In examining the locations of the parameters (see Table II in Appendix B) relative to the topological regions shown in Fig. 7, it appears the source of the asymmetry is the noticeable change in the value ϕ as R_a increases. This differs from the behavior when R_a decreases, where ϕ does not change substantially. This asymmetry in the transition points also occurs if instead R_a is fixed and R_b is adjusted. The main difference is that the spectral touching points switch from what was observed above: $K \leftrightarrow K'$.

VI. TOPOLOGICALLY PROTECTED EDGE MODES

The edge problem is now considered. An edge is placed along the zigzag edge parallel to the $\mathbf{v}_1$ lattice vector. Outside the semi-infinite strip, the electric field is assumed to decay exponentially fast. We find edge states that decay exponentially in the $\mathbf{v}_2$ direction. Two topologically distinct edge band diagrams are shown in Fig. 10. Edge modes along the direction $\mathbf{v}_1$ are found by taking

$$a_{mn}(t) = a_n(\mathbf{k})e^{i[m\mathbf{k}\cdot\mathbf{v}_1+\omega t]},$$

$$b_{mn}(t) = b_n(\mathbf{k})e^{i[m\mathbf{k}\cdot\mathbf{v}_1+\omega t]},$$

which reduces the governing system (6) and (7) to

$$\begin{aligned}\omega^2 a_n = {} & Pa_n + t_1[(1+e^{-i\mathbf{k}\cdot\mathbf{v}_1})b_n + b_{n-1}] \\ & + t_2 e^{i\phi}[a_{n+1} + e^{-i\mathbf{k}\cdot\mathbf{v}_1}a_n + e^{i\mathbf{k}\cdot\mathbf{v}_1}a_{n-1}] \\ & + t_2 e^{-i\phi}[a_{n-1} + e^{i\mathbf{k}\cdot\mathbf{v}_1}a_n + e^{-i\mathbf{k}\cdot\mathbf{v}_1}a_{n+1}] \end{aligned} \tag{18}$$

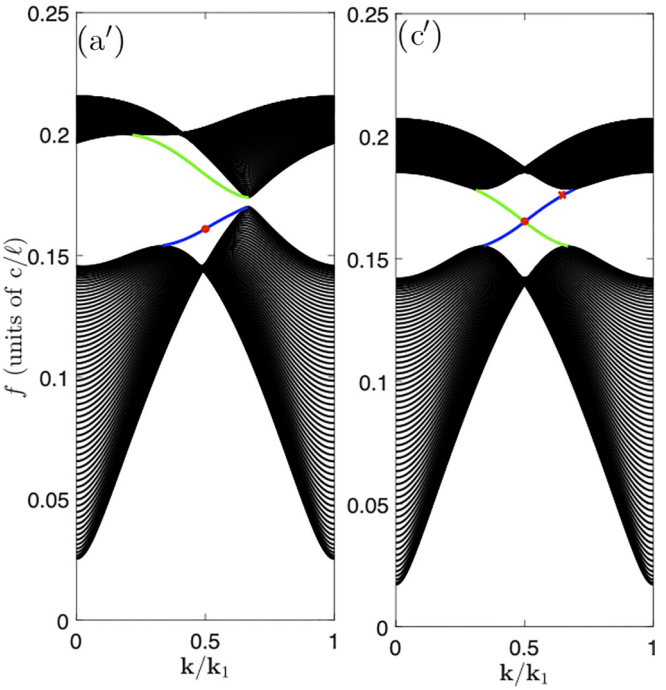

FIG. 10. Spectral edge bands parallel to the $\mathbf{v}_1$ zigzag edge. The model parameters for the (a′) topologically trivial and (c′) topologically nontrivial band diagrams are the same as those in Figs. 8(a) and 8(d), respectively. Green (blue) curves correspond to edge modes localized along the top (bottom) boundary, decaying in the $+\mathbf{v}_2$ ($-\mathbf{v}_2$) direction.

$$\omega^2 b_n = \widetilde{P} b_n + t_1[(1+e^{i\mathbf{k}\cdot\mathbf{v}_1})a_n + a_{n+1}] + \tilde{t}_2 e^{-i\phi}[b_{n+1} + e^{-i\mathbf{k}\cdot\mathbf{v}_1} b_n + e^{i\mathbf{k}\cdot\mathbf{v}_1} b_{n-1}] + \tilde{t}_2 e^{i\phi}[b_{n-1} + e^{i\mathbf{k}\cdot\mathbf{v}_1} b_n + e^{-i\mathbf{k}\cdot\mathbf{v}_1} b_{n+1}] \quad (19)$$

Note that $\mathbf{k}\cdot\mathbf{v}_1 = (r\mathbf{k}_1 + s\mathbf{k}_2)\cdot\mathbf{v}_1 = 2\pi r$ for $r, s \in \mathbb{R}$ due to the relationship $\mathbf{k}_i \cdot \mathbf{v}_j = 2\pi\delta_{ij}$. As a result, the coefficients cover one period over $0 \leqslant r \leqslant 1$. This system is solved numerically by implementing zero Dirichlet (open) boundary conditions

$$a_n, b_n = 0, \quad n < 1, n > N,$$

where N is taken to be large. We took $N = 64$ to generate Fig. 10. The band-gap eigenfunctions are exponentially localized and decay rapidly away from the boundary wall, in the $\pm\mathbf{v}_2$ direction.

The band configuration in Fig. 10(a′) corresponds to bulk eigenmodes with zero Chern number due to strong inversion symmetry breaking. As a result, there are no edge modes spanning the entire frequency gap. On the other hand, the system with corresponding nonzero Chern numbers in Fig. 10(c′) exhibits a nontrivial band structure inside the gap. These topologically protected chiral states propagate unidirectionally.

We consider time evolutions of these topologically distinct states. To do so, envelope approximations are evolved by taking the quasi-monochromatic initial data

$$a_{mn}(0) = \mathrm{sech}(\nu m) e^{im\bar{\mathbf{k}}\cdot\mathbf{v}_1} a_n(\bar{\mathbf{k}})$$
$$b_{mn}(0) = \mathrm{sech}(\nu m) e^{im\bar{\mathbf{k}}\cdot\mathbf{v}_1} b_n(\bar{\mathbf{k}}),$$

where a_n, b_n are numerically computed edge states indicated by the red dots at $\bar{\mathbf{k}} = 0.5\mathbf{k}_1$ in Fig. 10 and ν is a relatively small parameter; here, we took $\nu = 0.1$. Edge eigenmodes localized along the bottom edge of MO honeycomb lattice are taken. The edge envelopes are then propagated into a defect barrier missing two lattice cells in the $-\mathbf{v}_2$ direction, in which the electric field is negligibly small.

Using the initial condition above, the evolutions obtained by solving (6) and (7) are highlighted in Fig. 11. Edge states with corresponding nontrivial Chern invariants [see Figs. 10(c′) and 11(c″)] propagate chiraly around the defect barrier. There is virtually no loss in amplitude. On the other hand, edge modes associated with zero Chern number [see Figs. 10(a′) and 11(a″)] experience significant losses and scattering upon collision with the barrier. A portion of the original envelope propagates around the barrier, but there is a nearly 67% amplitude loss due to scattering into the bulk.

As a final note, we observe small decay in the maximal amplitude of these topologically protected modes, a roughly 10% decline over 1500 time units. This is expected due to dispersion. It is well known that self-focusing nonlinearity can balance these dispersive effects and form solitons [38]. This motivates this next section, which investigates a nonlinear Haldane model and edge solitons.

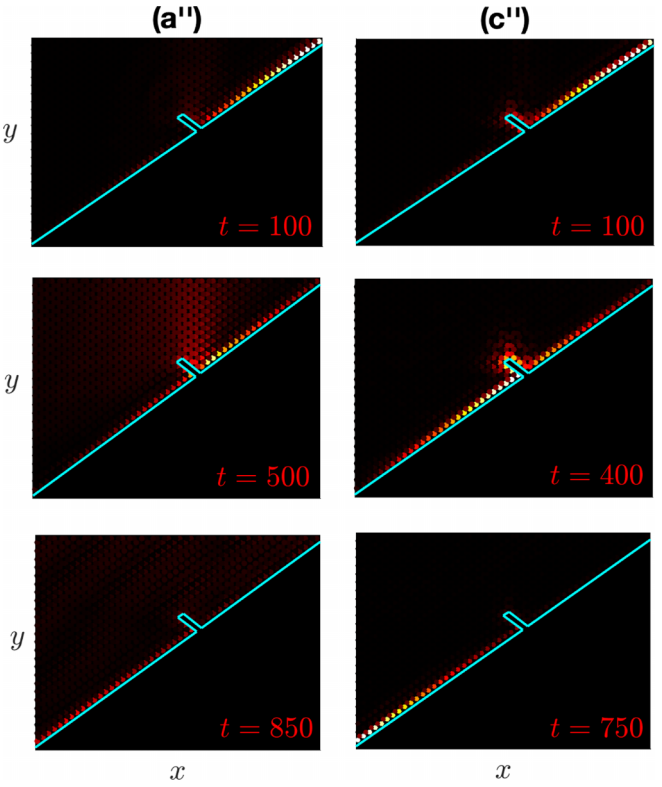

FIG. 11. Envelope evolutions along and through a defect barrier. Shown are both magnitudes $|a_{mn}(t)|$ and $|b_{mn}(t)|$ at times in units of ℓ/c. Shown are (a″) trivial and (c″) nontrivial Chern insulators with band diagrams given in Figs. 10(a′) and 10(a′), respectively. Note: brightness is relative to the $t = 100$ magnitude. The boundary is illustrated in teal color.

VII. A NONLINEAR HALDANE MODEL

In this section we consider the effects of nonlinearity in our Haldane model. The physical motivation here is that of a (relatively) high power electric field with nonnegligible on-site Kerr-type terms proportional to the field intensity. We consider the following nonlinear Haldane model:

$$\frac{d^2 a_{mn}}{dt^2} + P a_{mn} + t_1(\delta_- b_{mn}) + \sigma|a_{mn}|^2 a_{mn} + t_2 e^{i\phi}(\Delta_1 a_{mn}) + t_2 e^{-i\phi}(\Delta_2 a_{mn}) = 0 \quad (20)$$

$$\frac{d^2 b_{mn}}{dt^2} + \widetilde{P} b_{mn} + t_1(\delta_+ a_{mn}) + \sigma|b_{mn}|^2 b_{mn} + \tilde{t}_2 e^{-i\phi}(\Delta_1 b_{mn}) + \tilde{t}_2 e^{i\phi}(\Delta_2 b_{mn}) = 0, \quad (21)$$

where the linear interaction coefficients, $\delta_\pm$, Δ_j, $j = 1, 2$, are defined below Eqs. (6) and (7). Motivated by previous studies, we take an on-site focusing, Kerr-type nonlinearity, i.e., $\sigma > 0$. For the simulations below, we took $\sigma = 0.1$.

The initial conditions used to generate solitons below are of the form

$$a_{mn}(0) = A\,\mathrm{sech}(\nu m) e^{im\bar{\mathbf{k}}\cdot\mathbf{v}_1} a_n(\bar{\mathbf{k}})$$
$$b_{mn}(0) = A\,\mathrm{sech}(\nu m) e^{im\bar{\mathbf{k}}\cdot\mathbf{v}_1} b_n(\bar{\mathbf{k}}),$$

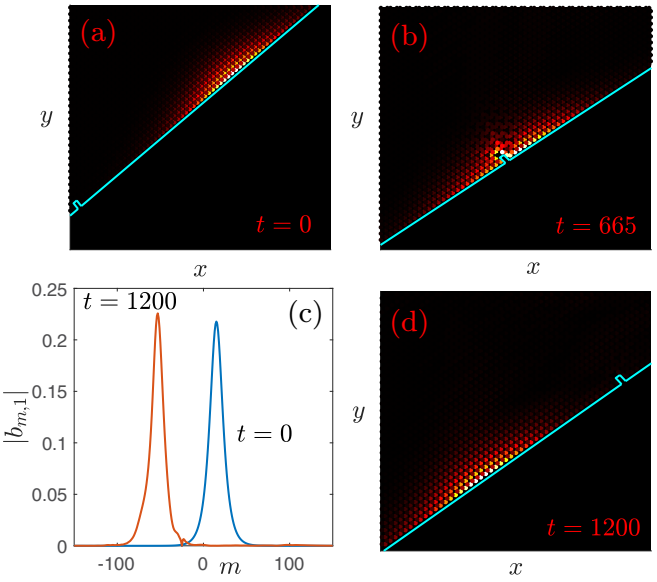

FIG. 12. Nonlinear edge soliton evolutions through a defect. (a), (b), (d) Both magnitudes $|a_{mn}(t)|$ and $|b_{mn}(t)|$ at times in units of ℓ/c. Note: brightness is relative to the $t = 0$ magnitude. The boundary is illustrated in teal color; the defect location is fixed. (c) Edge profile at the initial and final times.

with $\bar{\mathbf{k}} = 0.65\mathbf{k}_1$, and a_n, b_n are topologically nontrivial linear eigenmodes. We choose a linear edge mode whose corresponding dispersion (second derivative) is nonzero, i.e., $\omega''(\bar{\mathbf{k}}) \approx -0.287 < 0$ (see red "x" marker in Fig. 10). Note that these derivatives are defined in the directional derivative sense

$$\omega'(\mathbf{k}) = \nabla\omega|_{\mathbf{k}_1} = \lim_{h\to 0} \frac{\omega(\mathbf{k} + h\mathbf{k}_1) - \omega(\mathbf{k})}{h}.$$

For reference, the group velocity is $\omega'(\bar{\mathbf{k}}) \approx -0.0584$ in the $\mathbf{v}_1$ direction. Unfortunately, the third-order dispersion is relatively large, $\omega'''(\bar{\mathbf{k}}) \approx -1.401$, which will impact the formation of solitons. For this relatively weak dispersion, we seek a comparable weak nonlinearity to balance it, i.e., $A = 0.3$. A corresponding slowly varying profile ($\nu = 0.15$) is chosen to ensure as pure of a single edge mode as possible is excited.

Using the parameters described above, a typical evolution thorough a one-lattice cell defect in the $-\mathbf{v}_2$ direction is highlighted in Fig. 12. The resulting nonlinear mode propagates over relatively long time scales ($0 \leqslant t \leqslant 1200$) with a nearly constant solitary form. We observe a small 3.7% relative change in maximum magnitude between the initial and final states. Hence, we refer to this as an edge soliton. We note that, eventually, on longer time scales higher-order dispersion terms will become nonnegligible and the mode will degrade.

Now some further remarks about these topologically protected edge solitons. Choosing the appropriate sign of dispersion is imperative for achieving a self-focusing effect and solitons. When $\omega''(\mathbf{k}) > 0$, we observe a gradual self-defocusing dissipation of the envelope. The ideal scenario for soliton formation in this MO lattice is when $\omega''(\mathbf{k}) < 0$ and $\omega'''(\mathbf{k}) \approx 0$. Choosing a mode centered at the zero-dispersion (inflection) point, i.e., $\omega''(\mathbf{k}) = 0$, results in substantial dispersive breakup of initially localized solitary waves.

In the nonlinear case, when we send a slowly modulated mode corresponding to topologically trivial (null Chern number) into a defect, we observe significant radiation into the bulk, similar to that observed in Fig. 11(c′′). In this weakly nonlinear regime, it is important to modulate a topologically nontrivial linear mode to obtain robust, unidirectional propagation.

This model of nonlinearity is motivated by third-order polarization effects of the electric field that are significant [38]. These results suggest that it may be possible to realize nonlinear edge modes. One potential benefit of nonlinearity is the ability to (in theory) propagate balanced solitary modes over long time scales that do not suffer from dispersion. A complete description of these nonlinear modes is outside the scope of this work.

VIII. CONCLUSION

A perturbed Wannier approach for obtaining tight-binding approximations containing nearest and next-nearest neighbors of a magneto-optical honeycomb lattice system is studied. Remarkably, this method leads to a generalization of the celebrated system studied by Haldane in 1988 [11]. This model agrees with experiments [22] and indicates topological transitions can occur when inversion symmetry and time-reversal symmetry are broken. This data-driven Wannier approach has been previously employed in rectangular lattice geometries [27] and can be applicable for discovering and extrapolating discrete reductions in other Chern insulator systems in cases where a direct Wannier approach is ineffective. An interesting future project is to better understand the physical mechanisms that underlie this photonic Haldane model. When weak on-site nonlinearity is incorporated, we found that slowly varying edge soliton modes can be robustly propagated through lattice defects.

ACKNOWLEDGMENTS

This project was supported by the Air Force Office of Scientific Research (AFOSR). M.J.A. was partially supported under Grant No. FA9550-19-1-0084. J.T.C. was partially supported by Grant No. FA9550-23-1-0105.

APPENDIX A: NUMERICAL COMPUTATION OF SPECTRAL BANDS AND WANNIER FUNCTIONS

The numerical computation of the Bloch modes and MLWFs is reviewed below. A more comprehensive discussion can be found in Ref. [27]. To simplify the necessary calculations, first, a linear transformation is introduced to map the parallelogram unit cell to a square. The change of variables

$$u = \frac{1}{3}x - \frac{1}{\sqrt{3}}y, \quad v = \frac{1}{3}x + \frac{1}{\sqrt{3}}y$$

transforms the parallelogram formed by the lattice vectors $\mathbf{v}_1, \mathbf{v}_2$ into a square with (nondimensionalized) side length 1.

As a result, the master equation (2) transforms to

$$-\frac{4}{9}\left(\frac{\partial^2 E}{\partial u^2}-\frac{\partial^2 E}{\partial u\partial v}+\frac{\partial^2 E}{\partial v^2}\right)+g(u,v)\frac{\partial E}{\partial u}+h(u,v)\frac{\partial E}{\partial v}$$
$$=\omega^2\varepsilon(u,v)\tilde{\mu}(u,v)E, \tag{A1}$$

where

$$g(u,v)=\frac{4}{9\tilde{\mu}}\frac{\partial\tilde{\mu}}{\partial u}-\frac{2}{9\tilde{\mu}}\frac{\partial\tilde{\mu}}{\partial v}+\frac{2i\tilde{\mu}}{3\sqrt{3}}\frac{\partial\eta}{\partial v}$$
$$h(u,v)=-\frac{4}{9\tilde{\mu}}\frac{\partial\tilde{\mu}}{\partial u}+\frac{2}{9\tilde{\mu}}\frac{\partial\tilde{\mu}}{\partial v}-\frac{2i\tilde{\mu}}{3\sqrt{3}}\frac{\partial\eta}{\partial v}.$$

From here, a formulation similar to that used in Ref. [27] can be applied. All transformed coefficients now have the periodicity $f(u+m,v+n)=f(u,v)$ for $m,n\in\mathbb{Z}$. That is, the functions are periodic with respect to the transformed lattice vectors $\mathbf{e}_1=(1,0)^T$ and $\mathbf{e}_2=(0,1)^T$. Hence, transformed master equation (A1) is solved by looking for Bloch wave solutions with the form $E(\mathbf{w},\boldsymbol{\kappa})=e^{i\boldsymbol{\kappa}\cdot\mathbf{w}}u(\mathbf{w};\boldsymbol{\kappa})$, where $u(\mathbf{w}+m\mathbf{e}_2+n\mathbf{e}_1;\boldsymbol{\kappa})=u(\mathbf{w};\boldsymbol{\kappa})$ for $\mathbf{w}=(u,v)^T$, $\boldsymbol{\kappa}=(k_u,k_v)^T$. Note that this $\boldsymbol{\kappa}$ is unrelated to κ of the permeability tensor.

The numerical spectral bands shown throughout this paper are computed by solving (A1) for the eigenfunction-eigenvalue pair (u,ω) as functions of the transformed quasimomentum. Subsequently, the quasimomentum is transformed back to the original k_x,k_y variables via

$$k_x=\frac{k_u+k_v}{3},\quad k_y=\frac{k_v-k_u}{\sqrt{3}}.$$

The continuous Chern numbers are defined by

$$C_p=\frac{1}{2\pi i}\iint_{\mathrm{BZ}}(\nabla_{\mathbf{k}}\times\mathbf{A}_p)\cdot\hat{\mathbf{z}}d\mathbf{k},$$

with Berry connection

$$\mathbf{A}_p(\mathbf{k})=\langle u_p(\mathbf{r},\mathbf{k})|\partial_{k_x}u_p(\mathbf{r},\mathbf{k})\rangle_{\mathrm{UC},\epsilon\tilde{\mu}}\hat{\mathbf{x}}$$
$$+\langle u_p(\mathbf{r},\mathbf{k})|\partial_{k_y}u_p(\mathbf{r},\mathbf{k})\rangle_{\mathrm{UC},\epsilon\tilde{\mu}}\hat{\mathbf{y}}$$

numerically computed using the algorithm [37] with respect to the weighted inner product

$$\langle f,g\rangle_{\mathrm{UC},\epsilon\tilde{\mu}}=\iint_{\mathrm{UC}}f(\mathbf{r})^*g(\mathbf{r})\varepsilon(\mathbf{r})\tilde{\mu}(\mathbf{r})d\mathbf{r},$$

where UC denotes the unit cell.

The transformed Bloch wave is periodic with respect to the transformed reciprocal lattice vectors, $\boldsymbol{\kappa}_1=2\pi(1,0)^T$, $\boldsymbol{\kappa}_2=2\pi(0,1)^T$. Notice that $\mathbf{e}_i\cdot\boldsymbol{\kappa}_j=2\pi\delta_{ij}$. As such, it can be expressed as the Fourier series

$$E(\mathbf{w};\boldsymbol{\kappa})=\sum_p\sum_{m,n}W^p_{mn}(\mathbf{w})e^{i\boldsymbol{\kappa}\cdot(m\mathbf{e}_1+n\mathbf{e}_2)},$$

where $W^p_{mn}(\mathbf{w})$ is a transformed Wannier function corresponding to the pth band and centered at the (m,n) spatial cell. For the problem studied in this paper, we only consider the lowest two bands $p=1,2$ and truncate the remaining modes.

Next, the MLWF algorithm [36] is applied to find localized Wannier functions for the $g=h=0$ (corresponding to $\mathcal{M}=\mathbf{0}$) problem in Eq. (A1). This is done by finding a unitary transformation that minimizes the functional describing the spread of the Wannier function, given by Eq. (C1) below. Let $E_1(\mathbf{w},\boldsymbol{\kappa})=e^{i\boldsymbol{\kappa}\cdot\mathbf{w}}u_1(\mathbf{w};\boldsymbol{\kappa})$ and $E_2(\mathbf{w},\boldsymbol{\kappa})=e^{i\boldsymbol{\kappa}\cdot\mathbf{w}}u_2(\mathbf{w};\boldsymbol{\kappa})$ correspond to first and second spectral bands, respectively. A spectral unitary transformation of the Bloch functions is taken at fixed values of $\mathbf{w}$,

$$\begin{pmatrix}\widetilde{u}^c(\mathbf{w};\boldsymbol{\kappa})\\ \widetilde{u}^d(\mathbf{w};\boldsymbol{\kappa})\end{pmatrix}=\mathbb{U}(\boldsymbol{\kappa})\begin{pmatrix}u_1(\mathbf{w};\boldsymbol{\kappa})\\ u_2(\mathbf{w};\boldsymbol{\kappa})\end{pmatrix},$$

where $\mathbb{U}(\boldsymbol{\kappa})$ is a 2×2 matrix. Only after computing these Wannier functions do we realize where they are physically located. Upon inspection, we replace the labels c,d with the labels a,b, where a modes are centered at the a sites and b modes centered at the b sites (see Fig. 4).

Upon obtaining these functions, the Bloch modes $\widetilde{E}^a(\mathbf{w};\boldsymbol{\kappa})=e^{i\boldsymbol{\kappa}\cdot\mathbf{w}}\widetilde{u}^a(\mathbf{w};\boldsymbol{\kappa})$ and $\widetilde{E}^b(\mathbf{w};\boldsymbol{\kappa})=e^{i\boldsymbol{\kappa}\cdot\mathbf{w}}\widetilde{u}^b(\mathbf{w};\boldsymbol{\kappa})$ are computed and then used to construct the Wannier functions

$$\widetilde{W}^a_{mn}(\mathbf{w})=\frac{1}{4\pi^2}\iint_{\mathrm{BZ}}e^{-i\boldsymbol{\kappa}\cdot(m\mathbf{e}_1+n\mathbf{e}_2)}\widetilde{E}^a(\mathbf{w};\boldsymbol{\kappa})d\boldsymbol{\kappa}$$
$$\widetilde{W}^b_{mn}(\mathbf{w})=\frac{1}{4\pi^2}\iint_{\mathrm{BZ}}e^{-i\boldsymbol{\kappa}\cdot(m\mathbf{e}_1+n\mathbf{e}_2)}\widetilde{E}^b(\mathbf{w};\boldsymbol{\kappa})d\boldsymbol{\kappa}$$

shown in Fig. 4.

APPENDIX B: TIGHT-BINDING PARAMETERS

The self-interaction terms in the generalized Haldane model (6) and (7) are defined by

$$P=\iint_{\mathbb{R}^2}\nabla\widetilde{W}^a_{mn}\cdot\nabla\widetilde{W}^a_{mn}+\widetilde{W}^a_{mn}\,\mathcal{M}\cdot\nabla\widetilde{W}^a_{mn}\,d\boldsymbol{w} \tag{B1}$$

and

$$\widetilde{P}=\iint_{\mathbb{R}^2}\nabla\widetilde{W}^b_{mn}\cdot\nabla\widetilde{W}^b_{mn}+\widetilde{W}^b_{mn}\,\mathcal{M}\cdot\nabla\widetilde{W}^b_{mn}\,d\boldsymbol{w}. \tag{B2}$$

The nearest-neighbor coefficients in (6)and (7) are defined by

$$t_1=\iint_{\mathbb{R}^2}\nabla\widetilde{W}^a_{mn}\cdot\nabla\widetilde{W}^b_{mn}+\widetilde{W}^a_{mn}\,\mathcal{M}\cdot\nabla\widetilde{W}^b_{mn}\,d\boldsymbol{w}$$
$$=\iint_{\mathbb{R}^2}\nabla\widetilde{W}^b_{mn}\cdot\nabla\widetilde{W}^a_{mn}+\widetilde{W}^b_{mn}\,\mathcal{M}\cdot\nabla\widetilde{W}^a_{mn}\,d\boldsymbol{w}. \tag{B3}$$

TABLE II. Tight-binding parameters and Chern number in (6) and (7) for (i) nonmagnetized bands and (ii–viii) magnetized systems. The rod radii used to generate these parameters are given by R_a and R_b for a sites and b sites, respectively. The value of C_+ indicates the Chern number corresponding to the second (upper) spectral band. Cases (iii), (iv), (vi), and (vii) correspond to borderline touching cases, numerical calculation of the Chern number is sensitive in this region.

	R_a	R_b	P	$\widetilde{P}$	t_1	t_2	$\tilde{t}_2$	ϕ	C_+
(i)	0.3ℓ	0.3ℓ	0.882	0.882	−0.262	0.012	0.012	π	0
(ii)	0.3ℓ	0.3ℓ	1.020	1.020	−0.280	0.041	0.041	2.327	−1
(iii)	0.27ℓ	0.3ℓ	1.152	0.991	−0.297	0.049	0.037	2.391	−1*
(iv)	0.255ℓ	0.3ℓ	1.231	0.978	−0.311	0.053	0.035	2.444	0*
(v)	0.25ℓ	0.3ℓ	1.263	0.973	−0.300	0.055	0.030	2.405	0
(vi)	0.35ℓ	0.3ℓ	0.876	1.077	−0.265	0.031	0.048	2.178	−1*
(vii)	0.4ℓ	0.3ℓ	0.790	1.132	−0.263	0.024	0.053	1.941	0*
(viii)	0.42ℓ	0.3ℓ	0.729	1.149	−0.285	0.022	0.054	1.725	0

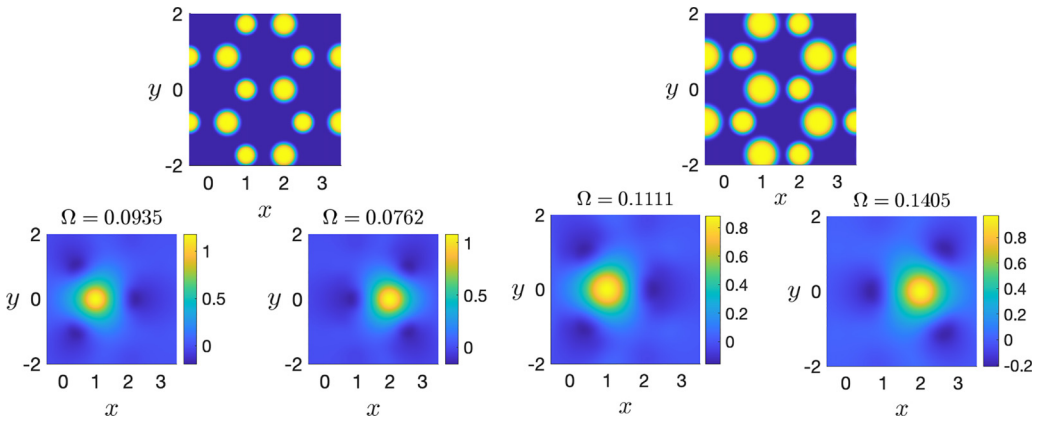

FIG. 13. The top row panels highlight the rod radii for the different cases. Bottom rows show the MLWFs corresponding to those physical parameters. (left) Radii: $R_a = 0.25\ell, R_b = 0.3\ell$ and (right) radii: $R_a = 0.4\ell, R_b = 0.3\ell$. Also included for each Wannier function is the corresponding spread, defined in (C1).

Both the self and nearest-neighbor coefficients were numerically computed using the Wannier functions in Fig. 4 and observed to be real. This process is highlighted in Fig. 5. One of the (complex) next-nearest-neighbor coefficients in the $\Delta_1 a_{mn}$ group of (6) is given by

$$t_2 e^{i\phi} = \iint_{\mathbb{R}^2} \nabla \widetilde{W}^a_{mn} \cdot \nabla \widetilde{W}^a_{m,n+1} + \widetilde{W}^a_{mn}\, \mathcal{M} \cdot \nabla \widetilde{W}^a_{m,n+1}\, d\boldsymbol{w}, \tag{B4}$$

where the left-hand side is written in polar form, i.e., $t_2 \geqslant 0$ is the magnitude and $\phi \in [0, 2\pi)$ is the phase. The other two coefficients of $\Delta_1 a_{mn}$ are calculated in a similar way. The coefficients for the terms in $\Delta_2 a_{mn}$ of (6) are also approximations of the integral of the relevant Wannier functions, but they are conjugates of those from $\Delta_1 a_{mn}$, hence they are labeled $t_2 e^{-i\phi}$. All the coefficients in (7) were computed in an analogous manner, using the $\widetilde{W}^b_{mn}$ Wannier modes.

The parameters generated by this method and used to produce the figures throughout this paper are given in Table II. All cases correspond to the magnetization by an external field, or $\mathcal{M}(\mathbf{r}) \neq \mathbf{0}$, except (i), which is the unmagnetized case. Also included are the corresponding rod radii. The Chern number corresponding to the upper spectral surface of the tight-binding model is included. The value $C_+ = -1$ corresponds to phase points located inside the topological region of Fig. 7, while $C_+ = 0$ lies above or below this region. The Chern numbers in the table were computed analytically as well as numerically using the algorithm in Ref. [37] on the discrete eigenvectors. The topological numbers for the discrete (tight-binding) model match those for the continuum model in the cases shown.

APPENDIX C: BREAKING OF INVERSION SYMMETRY

As discussed in Sec. V, breaking inversion symmetry can induce a topological transition from a nontrivial to trivial Chern insulator. This symmetry breaking can be implemented by choosing different radii at a sites and b sites, that is, $R_a \neq R_b$ in Fig. 1. The spectral bands induced by this change are shown in Figs. 8 and 9. In particular, decreasing R_a relative to R_b induces a topological transition and a touching point at the K Dirac point. If, on the other hand, one considers R_a larger relative to R_b, a similar topological transition occurs, but instead the gap closes at the opposite Dirac point, $K' = -K$.

The computed parameters are summarized in Table II. Examining the inversion parameter $M = (P - \widetilde{P})/2$, it is observed to be positive when $R_a < R_b$, and negative when $R_a > R_b$. For applications which seek to use these chiral edge modes, inversion symmetry should be nearly satisfied, that is, $R_a \approx R_b$. More precisely, the system supports topologically protected modes when the parameters M and ϕ are chosen to reside in the inner (topological) region of Fig. 7.

Some of the Wannier functions corresponding to broken inversion symmetry are shown in Fig. 13. In each case the rod profiles and their corresponding Wannier modes are shown. These Wannier modes are constructed in a manner similar to that described in Sec. III and [27], i.e., $\mathcal{M} = \mathbf{0}$, $\tilde{\mu} \neq \mu_0$. Also given is the corresponding spread values

$$\Omega = \langle |\mathbf{r}|^2 \rangle - |\langle \mathbf{r} \rangle|^2,$$
$$\langle x^n \rangle \equiv \iint_{\mathbb{R}^2} x^n |W(\mathbf{r})|^2 \varepsilon(\mathbf{r}) \tilde{\mu}(\mathbf{r}) d\mathbf{r}, \tag{C1}$$

where $W(\mathbf{r})$ is the associated Wannier mode. The sublattice sites whose rods have *larger* relative radius correlate to a *smaller* variances; and vice versa for smaller relative rods. This is the source of $\tilde{t}_2 \neq t_2$ and $P \neq \widetilde{P}$ in the tight-binding model. These different widths indicate different decay rates and imply different tight-binding coefficients among sites of the same type. On the other hand, the combined spreads for Fig. 13 (left) are smaller (narrower width) relative to Fig. 13 (right).

[1] G. Jotzu, M. Messer, R. Desbuquois, M. Lebrat, T. Uehlinger, D. Greif, and T. Esslinger, Nature (London) **515**, 237 (2014).

[2] K. v. Klitzing, G. Dorda, and M. Pepper, Phys. Rev. Lett. **45**, 494 (1980).

[3] B. A. Bernevig and S.-C. Zhang, Phys. Rev. Lett. **96**, 106802 (2006).
[4] C.-Z. Chang *et al.*, Science **340**, 167 (2013).
[5] P. Delplace, J. B. Marston, and A. Venaille, Science **358**, 1075 (2017).
[6] M. C. Rechtsman *et al.*, Nature (London) **496**, 196 (2013).
[7] T. Ozawa, H. M. Price, A. Amo, N. Goldman, M. Hafezi, L. Lu, M. C. Rechtsman, D. Schuster, J. Simon, O. Zilberberg, and I. Carusotto, Rev. Mod. Phys. **91**, 015006 (2019).
[8] L. Lu, J. D. Joannopoulos, and M. Soljačić, Nature Photon **8**, 821 (2014).
[9] M. J. Ablowitz and J. T. Cole, Physica D **440**, 133440 (2022).
[10] C. L. Fefferman, J. P. Lee-Thorp, and M. I. Weinstein, Comm. Pure Appl. Math. **71**, 1178 (2018).
[11] F. D. M. Haldane, Phys. Rev. Lett. **61**, 2015 (1988).
[12] S. Lannebère and M. G. Silveirinha, Phys. Rev. B **91**, 045416 (2015).
[13] S. Lannebère and M. G. Silveirinha, Phys. Rev. B **97**, 165128 (2018).
[14] S. Lannebère and M. G. Silveirinha, Nanophotonics **8**, 1387 (2019).
[15] M. J. Ablowitz, J. T. Cole, and S. D. Nixon, SIAM J. Appl. Math. **83**, 1623 (2023).
[16] Z. Wang, Y. D. Chong, J. D. Joannopoulos, and M. Soljačić, Phys. Rev. Lett. **100**, 013905 (2008).
[17] Z. Wang, Y. D. Chong, J. D. Joannopoulos, and M. Soljačić, Nature (London) **461**, 772 (2009).
[18] X.-C. Sun, C. He, X.-P. Liu, Y. Zou, M.-H. Lu, X. Hu, and Y.-F. Chen, Crystals **9**, 137 (2019).
[19] Y. Yang, Y. Poo, R.-X. Wu, Y. Gu, and P. Chen, Appl. Phys. Lett. **102**, 231113 (2013).
[20] X. Ao, Z. Lin, and C. T. Chan, Phys. Rev. B **80**, 033105 (2009).
[21] T. Ochiai and M. Onoda, Phys. Rev. B **80**, 155103 (2009).
[22] Y. Poo, R.-X. Wu, Z. Lin, Y. Yang, and C. T. Chan, Phys. Rev. Lett. **106**, 093903 (2011).
[23] R. Zhao, G.-D. Xie, M. L. N. Chen, Z. Lan, Z. Huang, and W. E. I. Sha, Opt. Express **28**, 4638 (2020).
[24] F. D. M. Haldane and S. Raghu, Phys. Rev. Lett. **100**, 013904 (2008).
[25] S. Raghu and F. D. M. Haldane, Phys. Rev. A **78**, 033834 (2008).
[26] J. P. Lee-Thorp, M. I. Weinstein, and Y. Zhu, Arch. Ration. Mech. Anal. **232**, 1 (2019).
[27] M. J. Ablowitz and J. T. Cole, Phys. Rev. A **101**, 023811 (2020).
[28] C. Brouder, G. Panati, M. Calandra, C. Mourougane, and N. Marzari, Phys. Rev. Lett. **98**, 046402 (2007).
[29] M. J. Ablowitz, C. W. Curtis, and Y.-P. Ma, Phys. Rev. A **90**, 023813 (2014).
[30] M. J. Ablowitz and J. T. Cole, Phys. Rev. A **96**, 043868 (2017).
[31] M. J. Ablowitz, J. T. Cole, P. Hu, and P. Rosenthal, Phys. Rev. E **103**, 042214 (2021).
[32] S. Mukherjee and M. C. Rechtsman, Phys. Rev. X **11**, 041057 (2021).
[33] G. Harari *et al.*, Science **359**, eaar4003 (2018).
[34] X. Zhou, Y. Wang, D. Leykam, and Y. D. Chong, New J. Phys. **19**, 095002 (2017).
[35] D. M. Pozar, *Microwave Engineering*, 4th ed. (Wiley, New York, 2012).
[36] N. Marzari and D. Vanderbilt, Phys. Rev. B **56**, 12847 (1997).
[37] T. Fukui, Y. Hatsugai, and H. Suzuki, J. Phys. Soc. Jpn. **74**, 1674 (2005).
[38] M. J. Ablowitz, *Nonlinear Dispersive Waves* (Cambridge Press, Cambridge, 2011).